

Impact of Cloud-Base Turbulence on CCN Activation: CCN Distribution

WOJCIECH W. GRABOWSKI,^a LOIS THOMAS,^{b,c} AND BIPIN KUMAR^b

^a *Mesoscale and Microscale Meteorology Laboratory, National Center for Atmospheric Research, Boulder, Colorado*

^b *HPCS, Indian Institute of Tropical Meteorology, Ministry of Earth Sciences, Pune, India*

^c *Department of Atmospheric and Space Sciences, Savitribai Phule Pune University, Pune, India*

(Manuscript received 26 March 2022, in final form 17 July 2022)

ABSTRACT: Following our previous investigation of the turbulence impact on cloud-base single-size CCN activation, this study considers a similar problem assuming CCN size distribution obtained from field measurements. The total CCN concentration is taken as either 200 cm^{-3} to represent clean conditions, or as 2000 cm^{-3} to represent polluted conditions. CCN is assumed to be sodium chloride. The CCN activation in the rising nonturbulent adiabatic parcel is contrasted with the activation within a rising adiabatic parcel filled with inertial-range homogeneous isotropic turbulence. The turbulent parcel of 64^3 m^3 and the turbulent kinetic energy dissipation rate of $10^{-3} \text{ m}^{-2} \text{ s}^{-3}$ are used in most of the simulations. Results for a range of mean parcel ascent rates, between 0.125 and 8 m s^{-1} , are discussed. Overall, the adiabatic turbulent parcel simulations show results consistent with the adiabatic nonturbulent parcel, with higher activated CCN concentrations for stronger parcel ascent rates. The key difference is a blurriness of the separation between dry CCN size bins featuring activated and nonactivated (haze) CCN, especially for weak mean ascent rates. The blurriness comes from CCN getting activated and subsequently deactivated in the fluctuating supersaturation field, instead of all becoming cloud droplets above the cloud base. This leads to significantly larger spectral widths in turbulent parcel simulations compared to the nonturbulent parcel when activation is completed. Modeling results are discussed in the context of the impact of turbulent fluctuations on CCN activation documented in laboratory experiments using the Pi chamber.

KEYWORDS: Aerosols; Cloud microphysics; Cumulus clouds

1. Introduction

Cloud droplets in natural clouds form through activation of cloud condensation nuclei (CCN), submicron soluble aerosol particles abundant in Earth's atmosphere. For boundary layer clouds like stratocumulus and shallow cumulus, as well as for the deep convection, CCN activation takes place when boundary layer air rising toward the cloud base reaches water saturation. Characteristics of the cloud droplet population after the cloud-base CCN activation is completed (e.g., total droplet concentration, spectral width) affect cloud properties and eventual precipitation formation aloft.

A traditional approach to study cloud-base CCN activation is to consider adiabatic parcel rising through the cloud base (e.g., Pruppacher and Klett 1997; Reutter et al. 2009; Pinsky et al. 2013; see a comprehensive list of references in Ghan et al. 2011). The key motivation is to understand the impact of CCN physicochemical properties and cloud-base updraft speeds on the droplet concentration above the cloud base. Such an approach excludes possible impacts of cloud turbulence. Turbulence provides vertical velocity fluctuations that lead to local supersaturation fluctuations affecting CCN activation and droplet growth. Such a line of thought led to a study reported in Grabowski et al. (2022, hereafter G22) that considers the impact of turbulence on single-size cloud-base CCN activation. However, natural CCN typically occur in different sizes and often in different chemical compositions as documented in numerous studies (e.g., Jiusto 1967; Mészáros

1968; Fitzgerald 1973; Hoppel 1979; Hudson and Yum 2002; Miao et al. 2015). It follows that expanding the G22 study to the case of the CCN distribution is a logical next step.

It is well understood from the Köhler theory (Köhler 1936), that the critical (activation) supersaturation increases, and the critical (activation) radius decreases, with the decrease of the CCN particle dry mass (e.g., see Fig. 1 in G22 or Fig. 2 here). Therefore, when the adiabatic air parcel rises across the cloud base, the largest CCN can be activated first, and increasingly smaller CCN can be activated as the supersaturation continues to increase. However, there are important aspects that need to be kept in mind when discussing the cloud-base activation of the CCN spectrum. First, large CCN (say, with radius larger than 100 nm) feature large activation radii (above $1 \text{ }\mu\text{m}$) and thus need time to reach the critical radius (see, for instance, results for the 200-nm CCN radius simulations in G22's Fig. 3). Second, deliquesced large CCN lag behind, that is, their radius is smaller than the equilibrium radius for the supersaturation inside the rising parcel at a given level, and thus they need additional time to reach the critical radius. For instance, when passing the saturation level in the adiabatic parcel simulations with the mean updraft of 1 m s^{-1} discussed later in this paper, the 20-nm dry radius CCN has a deliquesced (wet) radius almost equal to the equilibrium radius of 111 nm ($0.111 \text{ }\mu\text{m}$). However, the 100-nm deliquesced CCN has the radius of about $0.85 \text{ }\mu\text{m}$, significantly smaller than the $1.20\text{-}\mu\text{m}$ equilibrium radius at water saturation (i.e., about 35% of the equilibrium mass). Finally, even if the local supersaturation passes the critical supersaturation and the droplet radius becomes larger than the critical radius, the eventual CCN activation and further growth of a cloud droplet are not guaranteed.

Corresponding author: Wojciech W. Grabowski, grabow@ucar.edu.

DOI: 10.1175/JAS-D-22-0075.1

For information regarding reuse of this content and general copyright information, consult the [AMS Copyright Policy \(www.ametsoc.org/PUBSReuseLicenses\)](https://www.ametsoc.org/PUBSReuseLicenses).

This is because the droplet radius growth rate is proportional to the difference between the local supersaturation and the Köhler-theory equilibrium supersaturation. It follows that the droplet with a radius larger than the critical radius may start evaporating once the local supersaturation drops below the equilibrium supersaturation for a given dry CCN radius. This aspect is discussed in detail in section 3 of Abade et al. (2018, see their Figs. 2 and 3); see also Arabas and Shima (2017). Such a growth reversal of an already-activated cloud droplet is especially relevant for the case of turbulent CCN activation because the local supersaturation is strongly affected by turbulent fluctuations when the mean parcel ascent is low. But it can also take place for the case of an adiabatic parcel when the supersaturation after activation is very low (for instance, because of a high droplet concentration in a polluted environment) as illustrated in this paper.

As the latent heat of condensation and the sink of water vapor due to growing droplets gradually increase, the supersaturation reaches its peak and starts to decrease. The peak supersaturation depends on the updraft speed alone given the CCN chemical composition and the CCN size distribution. For that reason, we consider a wide range of updrafts, from 0.125 to 8 m s⁻¹ and several values in between. For the adiabatic parcel, the total droplet concentration once activation is completed is determined by the CCN concentration from the largest CCN to the smallest activated CCN. In such a case, the boundary between activated and inactivated (haze or interstitial) CCN above the cloud base is sharp, that is, any given CCN is either activated or remains inactivated. All those features are well understood based on numerous past CCN activation studies applying the adiabatic rising parcel framework. Such a picture gets modified once the cloud turbulence is taken into consideration as discussed in this paper.

The same methodology as in G22 is used herein to study turbulence impact on the activation of a realistic (i.e., observed) CCN spectrum. For the readers' convenience, the next section provides a summary of G22 methodology and G22 results. Readers familiar with G22 can move directly to section 3 that describes specific aspects of the study reported here. Section 4 discusses results from simulations applying the adiabatic parcel framework. In addition to traditional aspects of the CCN activation, such as the relationship between the updraft strength and the concentration of cloud droplets once activation is completed, we investigate the evolution of the spectral width that is the key quantity for the evolution of the droplet spectra in undiluted cloud volumes above the cloud base. Section 5 discusses results from simulations of CCN activation within a turbulent parcel rising across the cloud base. The discussion in section 6 and the summary in section 7 conclude the paper.

2. Simulations of single-size CCN activation in G22

a. Methodology

The study reported in G22 compares CCN activation inside an adiabatic parcel rising through the cloud base with the activation inside an adiabatic parcel filled with the inertial-range

homogeneous isotropic turbulence.¹ In the adiabatic parcel, all CCN and cloud droplets (cloud particles) experience exactly the same supersaturation history. For the parcel filled with inertial-range turbulence, there are spatial fluctuations of the supersaturation field. As a result, all cloud particles followed in a turbulent parcel simulation experience variable supersaturation histories as in Cooper (1989). For the turbulent parcel, the Eulerian–semi-Lagrangian (EULAG) anelastic finite-difference fluid flow model (<http://www.mmm.ucar.edu/eulag/>) is applied in the implicit large eddy simulation (ILES) mode. ILES applies no explicit dissipation, and small-scale velocity and scalar fluctuations are removed through numerical diffusion provided by the monotone Eulerian advection scheme (Margolin and Rider 2002; Andrejczuk et al. 2004; Margolin et al. 2006; Grinstein et al. 2007). Inertial-range turbulence within the triply periodic computational domain is maintained by a variant of the linear forcing method that preserves the mean turbulent kinetic energy (TKE), see Grabowski and Thomas (2021) for details. Initial conditions for the adiabatic parcel simulations assume uniform 97% relative humidity (i.e., -3% supersaturation), uniform temperature of 283 K, and uniform pressure of 900 hPa. For the adiabatic turbulent parcel, initial temperature perturbations (from the 283-K mean) are taken from CCN-free simulations (i.e., no condensation) without the mean ascent run for a few eddy-turnover times. The initial water vapor perturbations (from the value corresponding to -3% supersaturation at the 283-K temperature) are locally calculated from temperature perturbations to ensure spatially uniform -3% supersaturation across the computational domain at the onset of the turbulent parcel simulations. Vertical velocity fluctuations due to turbulent motions inside the parcel induce dry-adiabatic temperature perturbations that drive supersaturation fluctuations. The parcel rises with a prescribed constant-in-time ascent rate that leads to a dry-adiabatic decrease of the mean parcel temperature (in addition to the turbulent fluctuations) and reduction of the mean pressure in agreement with the hydrostatic balance (see, for instance, Grabowski and Wang 2009 for the equations describing the adiabatic parcel). For the nonturbulent parcel, saturated conditions are reached after about 50 m of the parcel rise. Simulations continue up to the 200-m height.

Most simulations discussed in G22 considered a low TKE corresponding to the TKE dissipation rate of 10⁻³ m² s⁻³, arguably appropriate for the boundary layer air approaching the cloud base (e.g., Siebert et al. 2006; Borque et al. 2016). For the 64³-m³ computational domain considered in majority of the simulations in G22 and herein, the low TKE corresponds to the rms perturbation vertical velocity (i.e., excluding the prescribed mean ascent) of around 0.2 m s⁻¹ and fluctuating maximum vertical velocity between 0.5 and 0.8 m s⁻¹. The TKE is around 0.05 m² s⁻². Mean cloud-base updraft velocities that are prescribed independently of the TKE are assumed as 0.33, 1, and 3 m s⁻¹. Additional

¹ The “adiabatic turbulent parcel” phrase can be considered inappropriate because the simulations do assume an influx of the turbulent kinetic energy (TKE). However, the parcel remains adiabatic from the thermodynamics point of view (i.e., no entrainment). The same term was used in G22, Grabowski and Abade (2017), and Abade et al. (2018).

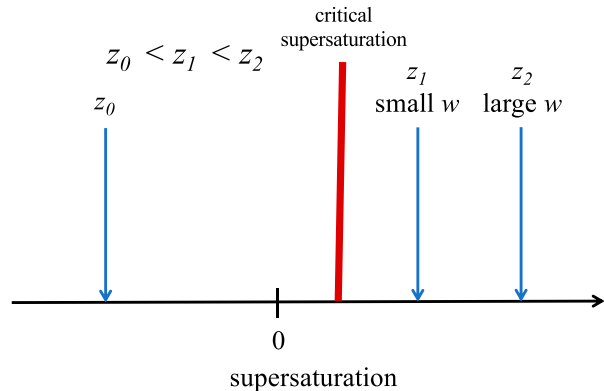
sensitivity simulations included either a lower TKE dissipation rate or a smaller computational domain.

The computational domain size together with the assumed TKE dissipation rate determine maximum turbulent velocities and thus the maximum time step [dictated by the Courant–Friedrichs–Lewy (CFL) stability criterion], that can be used in the dynamic simulations. Simulations discussed in G22 as well as in this paper typically apply the time step between 0.1 and 0.3 s. Since the droplet growth may require a smaller time step (especially for small CCN before activation), a simple substepping procedure is used to ensure that the microphysical time step used in the droplet growth calculation is sufficiently small. The procedure ensures that the time step to calculate droplet growth is not larger than 1/20 of the droplet growth characteristic time defined as the ratio of the droplet radius r to its rate of change, that is, r over dr/dt . The microphysical time step cannot be larger than the dynamic model time step. The adiabatic nonturbulent parcel simulations apply a 0.01-s time step with the same substepping procedure applied if needed.

In separate sets of simulations, G22 study considers two dry CCN sizes, small with the dry radius of 10 nm and large with the dry radius of 200 nm. Small CCN have the activation (critical) radius of $0.06 \mu\text{m}^2$ and the critical supersaturation of 1.3%. Large CCN feature activation radius of $5.4 \mu\text{m}$ and critical supersaturation 0.15%. CCN are assumed in 200-cm^{-3} concentrations in all simulations and are initially assumed at the equilibrium with the ambient -3% supersaturation. For the adiabatic turbulent parcel, a Lagrangian approach is used in the microphysics calculations in which a set of point particles representing deliquesced CCN and activated droplets is followed in the periodic computational domain. Because of the computational domain size, it is impossible to follow all particles and the so-called superdroplet method is used. In this approach, we use a computationally feasible total number of Lagrangian particles and assign each of them the multiplicity attribute that tells how many real CCN or cloud droplets each superdroplet represents. With the computational grid (64^3) and the number of superdroplets per grid volume (20 for all simulations in G22), the total number of particles followed in the computational domain is around 5.2 million. As in Grabowski and Thomas (2021), each superdroplet responds to the mean supersaturation within the grid volume corresponding to its location. The condensation rate needed for the Eulerian temperature and water vapor equations is obtained by summing up the mass change of all superdroplets within a given grid volume (see appendix B in Grabowski and Thomas 2021).

As discussed in the G22 appendix, the computational domain size determines supersaturation fluctuations before CCN activation commences. This is because the rate of change of the local temperature is proportional to the turbulent vertical velocity. Hence, the temperature change depends on the vertical displacement that is larger when the cubic domain is larger. Neither the range of scales (i.e., the simulation Reynolds number) nor the TKE dissipation rate (that determines the turbulent velocity fluctuations) are important for a given domain

(a) nonturbulent parcel



(b) turbulent parcel

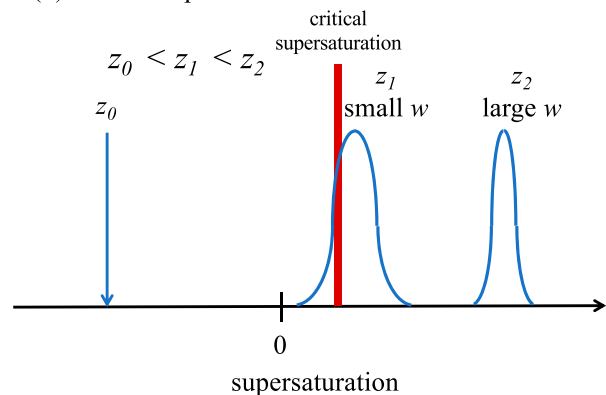


FIG. 1. Schematic representation of single-size CCN activation from G22. Horizontal axis is the evolving in time supersaturation. The mean updraft (assumed constant in time) is w . Starting height for the simulations is denoted as z_0 . See text for the discussion.

size as shown in Fig. A2 in G22. As G22's Fig. A2 shows, the supersaturation fluctuation standard deviation is around 0.1% for the cubic domain size of around 10^3 m^3 and it increases to about 1% for 100^3-m^3 domain. A few tenths of 1% supersaturation fluctuations are similar to those obtained from in situ observations discussed in Ditas et al. (2012). However, the vertical velocity fluctuations do affect supersaturation fluctuations once CCN become activated and turn into cloud droplets. This is because the supersaturation evolution comes from the combination of the vertical-velocity dry-adiabatic forcing and the sink due to cloud droplet growth (e.g., Squires 1952; Politovich and Cooper 1988).

b. Summary of G22 results

Figure 1 provides a schematic summarizing G22 results. The top panel illustrates activation within an adiabatic nonturbulent parcel. Activation within a turbulent parcel is schematically shown in the bottom panel.

For the nonturbulent parcel, the supersaturation increases as the parcel rises from the initial height z_0 . Once the

² That value was erroneously stated to be $0.6 \mu\text{m}$ in G22.

supersaturation surpasses the critical supersaturation, CCN activation becomes possible. For small CCN, activation takes place almost immediately after critical supersaturation is passed. Large CCN lag behind (i.e., their deliquesced size is smaller than the equilibrium size at a given supersaturation) and they reach the activation radius several tens of meters above the critical supersaturation level. For small and large CCN, the supersaturation continues to increase after passing the critical supersaturation, reaching higher values at larger heights for stronger updrafts. The supersaturation starts to decrease once the supersaturation sink due to cloud droplets growth overcomes the source due to the vertical velocity. For a given updraft and CCN size, all droplets at the 200-m height have the same size (i.e., zero spectral width). Droplet radii for small and large CCN are almost the same because both CCN are assumed to have the same concentration.

The critical difference for the turbulent parcel is that supersaturation fluctuations develop after the parcel begins to rise and they have a significant impact on the CCN activation. (The distributions show in the bottom panel of Fig. 1 are just a schematic; the distributions seen in numerical simulations are more complicated, see Fig. 6 in G22). Because of the fluctuations, the mean supersaturation does not have to reach the critical supersaturation for the activation to begin for both small and large CCN (Prabhakaran et al. 2020). This has a profound impact for the small CCN that can activate and deactivate rapidly when the supersaturation changes, especially for small prescribed parcel ascent rates. The latter is because the mean supersaturation after activation onset is smaller for smaller ascents and turbulent fluctuations can shift local supersaturation above or below the critical supersaturation easily, thus allowing activation and/or deactivation (e.g., Arabas and Shima 2017; Abade et al. 2018). Moreover, when the mean ascent rate is small, there is more time for activation/deactivation cycles. Another effect, seen only in simulations with small CCN, is that activation of only a fraction of all CCN is possible for low ascent rates. This is as in fluctuation-influenced and fluctuation-dominated activation regimes as proposed in Prabhakaran et al. (2020, see their Fig. 1). This leads to reduced droplet concentrations when activation is completed. For instance, for the 0.33 m s^{-1} (1 m s^{-1}) ascent, only about a quarter (80%) of all small CCN become activated in simulations with 64^3-m^3 domain. This is possible because large activation supersaturation for small CCN leads to rapid growth of cloud droplets after activation that provides a large sink for the mean supersaturation limiting the subsequent CCN activation. All those effects contribute to the finite activated droplet spectral width once activation is completed, between a few tenth of $1 \mu\text{m}$ to close to $2 \mu\text{m}$.

In summary, for the parcel without turbulence carrying either small or large CCN, all CCN are activated regardless of the updraft strength, and cloud droplets have the same size after activation (i.e., zero spectral width). In contrast, turbulence can lead to activation of only a fraction of the carried CCN, especially in the case of small CCN and weak mean cloud-base ascent. The droplet size distribution after turbulent activation is completed has a finite spectral width, on the order of $1 \mu\text{m}$.

3. Numerical simulations with CCN spectrum

We apply the same methodology as in G22. First, we use a traditional approach to study CCN activation, that is, an adiabatic rising parcel. Subsequently, we apply the adiabatic turbulent parcel framework introduced in G22 in several sets of simulations. A wider range of parcel mean ascent rates than in G22 is considered here: 0.125, 0.25, 0.5, 1, 2, 4, and 8 m s^{-1} . This is because the concentration of activated CCN strongly depends on the updraft speed, with only large CCN activated when the updraft is weak, and progressively smaller CCN activated for stronger updrafts. The initial conditions for a 200-m parcel displacement are as in G22: 97% relative humidity (i.e., -3% supersaturation), the mean temperature of 283 K, and pressure of 900 hPa. In the main set of simulations, a 64^3 m^3 computational domain as in G22 is used with 1-m grid length. Sensitivity simulations as in G22 are also included to document the impact of specific modeling assumptions. Details of sensitivity simulations are provided in section 5.

A single CCN distribution is selected for the study reported in this paper. The distribution comes from aircraft observations in one of the flights during the Variability of the American Monsoon Systems (VAMOS) Ocean-Cloud-Atmosphere-Land Study Regional Experiment (VOCALS-REX) as used in Grabowski et al. (2011, see their section 2). The distribution combines two lognormal modes centered at 20- and 75-nm radii (0.020 and $0.075 \mu\text{m}$, respectively), the geometric standard deviations of 1.4 and 1.6 (unitless), and total concentrations of 120 and 80 cm^{-3} , respectively. For the analysis presented here, the distribution is truncated to cover only the range between 2 and 200 nm (0.002 and $0.2 \mu\text{m}$). Smaller CCN are unlikely activated for typical cloud-base updrafts, and larger CCN (activated even for very weak updrafts due to their low critical supersaturation) contribute little to the total CCN concentration as illustrated below. Specific results presented in this paper likely depend to some extent on the assumed CCN spectral shape; this needs to be kept in mind while discussing the results. Although in low concentrations, larger (giant and ultra-giant) CCN may contribute to the development of rain through collision/coalescence (e.g., Johnson 1982; Feingold et al. 1999; Dziekan et al. 2021). However, droplet collisions are not considered. In the second set of simulations, the CCN concentrations for the two modes are increased by an order of magnitude, that is, to 1200 and 800 cm^{-3} , to illustrate the turbulence impact on CCN activation in polluted clouds. We will refer to these two sets of simulations as “ 200 cm^{-3} ” and “ 2000 cm^{-3} ” throughout the paper.

For numerical simulations, the assumed CCN distribution is discretized into equally spaced bins in the logarithmic scale. For the adiabatic parcel, the number of bins is equal to 120 and 1200 for 200 cm^{-3} and 2000 cm^{-3} , respectively. Such a high spectral resolution is needed to have the results independent from the selected number of bins (not shown). Each bin is represented by a single superdroplet with a multiplicity derived from the initial CCN distribution. Note that having 10 times more bins for the 2000 cm^{-3} cases compared to the 200 cm^{-3} cases implies that the number of real CCN represented by each superdroplet is approximately the same for the two cases. For the turbulent parcel simulations, the CCN distribution is

discretized into 30 equally spaced bins in the logarithmic scale, and the number of superdroplets is initially assumed 30 per grid volume. This allows a simple initialization of turbulent parcel simulations because each grid volume receives 30 superdroplets from the 30-bin distribution at the simulation onset. A superdroplet is put at a random position within each grid volume and is followed throughout the simulations. Our previous investigations applying superdroplet approach to study cloud droplet growth by condensation (Grabowski 2020a,b) show that such a number of superdroplets per grid volume is sufficient. The total number of superdroplets is around 7.8 million in each adiabatic turbulent parcel simulation.

4. CCN activation in the nonturbulent parcel

As in G22, we begin with results from the adiabatic parcel without turbulence to provide reference for the turbulent parcel simulations. Results of those simulations are illustrated in Figs. 3–6. Figure 3 documents evolutions of the supersaturation, mean droplet radius, and spectral width (the standard deviation of the droplet size distribution) for adiabatic parcels rising with 0.25, 1, and 4 m s⁻¹. The mean radius and spectral width are calculated including only droplets whose radius is larger than the activation radius shown in Fig. 2. Before the parcel reaches saturation, the supersaturation increases in the same way for the three updrafts because the adiabatic temperature decrease depends on the vertical displacement and not on the parcel ascent rate. For the 200 cm⁻³ case, CCN activation commences shortly after the parcel reaches saturation, and continues until the supersaturation reaches its peak, larger and farther away from the saturation level for stronger updrafts. The maximum supersaturation determines the smallest CCN that can be activated, smaller for stronger updrafts. For the same mean ascent, the supersaturation peak features higher supersaturation for the 200 cm⁻³ case than for the 2000 cm⁻³ case. The differences between the 200 and 2000 cm⁻³ sets include lower supersaturation peaks and smaller mean droplet radii for corresponding ascent rates, in agreement with numerous previous studies comparing CCN activation in clean and polluted CCN environments.

Spectral width evolutions differ between 200 and 2000 cm⁻³ cases. For the 200 cm⁻³ case, spectral width increases rapidly during activation, and then starts to decrease as the parcel continues to rise. A traditional explanation of the spectral width decrease after activation involves the droplet radius growth rate that is inversely proportional to the droplet radius, $dr/dt \sim 1/r$, that is, larger droplets growing slower and thus spectral width decreasing. However, such an argument assumes that the Köhler theory equilibrium supersaturation is small, that is, the Kelvin and Raoult effects can be neglected. For the 200 cm⁻³ simulations, droplets quickly reach sizes of several microns and the supersaturation continues to be relatively large, so the decrease of the spectral width after activation agrees with the traditional explanation [and with previous studies as shown, for example, in Grabowski et al. (2011, see their Fig. 4), Grabowski and Abade (2017, see their Fig. 2), and Abade et al. (2018, see their Fig. 5)]. In contrast, droplet radii and supersaturations are smaller for the 2000 cm⁻³ cases, and the traditional argument seems no longer valid. As a result, spectral widths for the

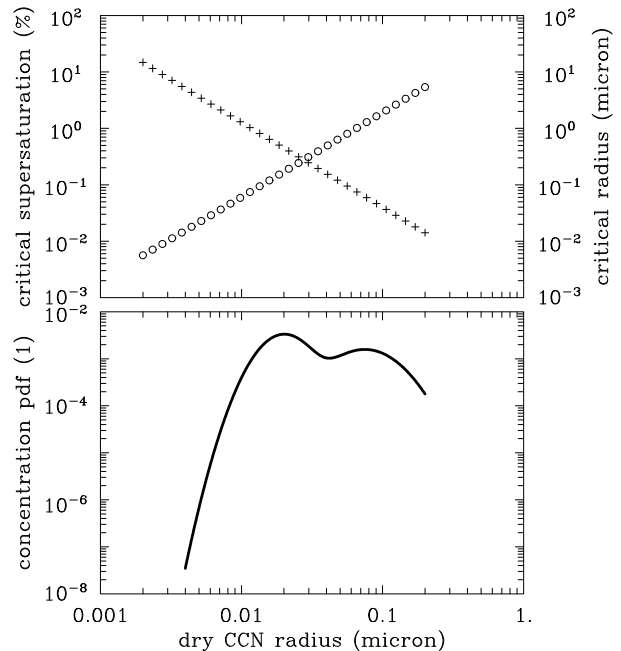


FIG. 2. (bottom) CCN distribution applied in simulations described in this paper. The distribution is not shown down to 2 nm (0.002 μm) as the values are smaller than the lowest value on the vertical axis. (top) Critical (activation) supersaturation (plus symbols) and critical (activation) radius (circles) as a function of the CCN dry radius. Horizontal scale is as in the bottom panel.

2000 cm⁻³ cases with 0.25 and 1 m s⁻¹ updrafts continue to increase up to 200-m height. One should expect a reversal of this trend once droplets become sufficiently large above the 200-m height and the simplified droplet growth equation becomes valid. There are also small “jumps” in the spectral width evolutions for those cases in the upper right panel. These come from droplets crossing the activation radius and becoming either included or excluded from the spectral width calculation. Note that even if a droplet radius is above the critical radius, the droplet will evaporate (grow) if the supersaturation is below (above) the equilibrium supersaturation corresponding to the droplet radius (see discussion in the introduction). These “jumps” are more apparent when lower bin resolution is used to represent CCN spectrum (not shown).

The above discussion is supported by the evolutions of the droplet concentration in all six simulations from Fig. 3 as shown in Fig. 4. For the 200 cm⁻³ case (solid lines in Fig. 4), droplet concentrations do not change after activation is completed. But for the 2000 cm⁻³ cases, droplet concentrations continue changing up to the simulation end. A steady increase of the droplet concentration between 100- and 200-m height for 4 m s⁻¹ updraft and a continuous decrease for 0.25 and 1 m s⁻¹ updrafts imply that the droplet activation/deactivation continues up to the end of the 2000 cm⁻³ simulations. This is consistent with the impact of smaller droplet sizes (making the Kelvin and Raoult effects nonnegligible) and smaller supersaturations (making them comparable to the Köhler theory equilibrium supersaturations) for the 2000 cm⁻³ polluted cases as discussed above.

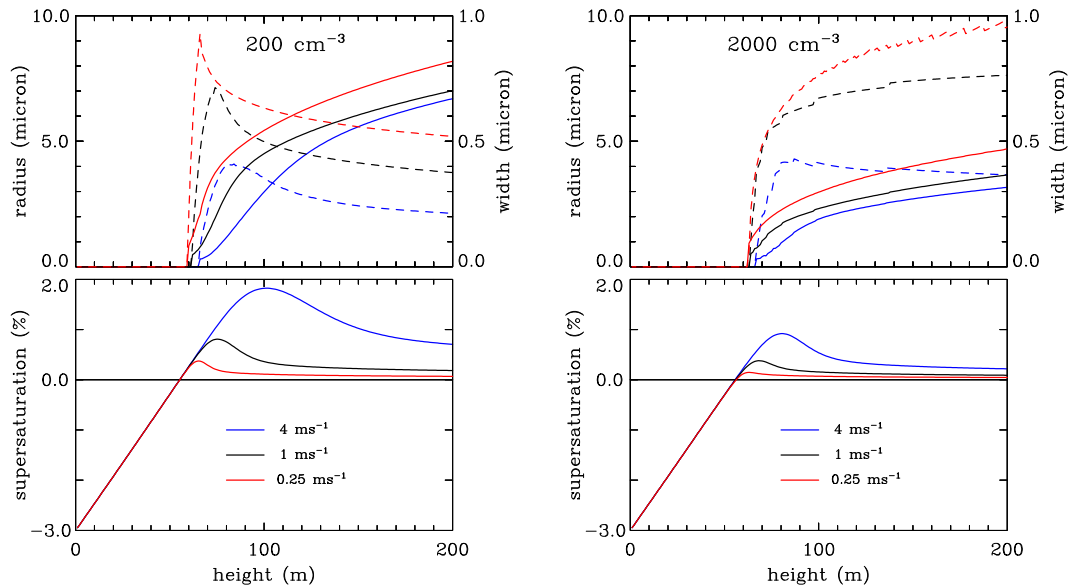


FIG. 3. Evolution of (bottom) supersaturation and (top) mean droplet radius (solid lines; left scale on vertical axis) and spectral width (dashed lines; right scale on vertical axis) for adiabatic parcel simulations with updraft velocities of 0.25, 1, and 4 m s^{-1} shown by different colors. (left) 200 and (right) 2000 cm^{-3} simulations.

Figure 5 shows final (i.e., at the 200-m height) droplet concentrations, mean radius, and spectral width as a function of the updraft speed. Only a fraction of the total CCN concentration is activated for weak updrafts. The fraction is close to the total concentration (i.e., 200 and 2000 cm^{-3} for the two simulation sets) for the strongest updrafts. The differences in the supersaturation peak between 200 and 2000 cm^{-3} sets are responsible for the differences in the droplet concentrations when scaled by the total CCN concentration ratio of 10. For instance, for the 1 m s^{-1} updraft, droplet concentration is around 180 cm^{-3} for the 200 cm^{-3} versus only 1200 cm^{-3} —rather than 1800 cm^{-3} —for 2000 cm^{-3} case. Note that such a comparison is only possible because of the same shape of the CCN size spectrum in 200 and 2000 cm^{-3} sets. Because the liquid water differs little

between all simulations at 200-m height (not shown), differences in the droplet concentration approximately explain differences in the final mean droplet radius. The final spectral widths, systematically larger for the 2000 cm^{-3} simulations, are between a few tenths of 1 μm and close to 1 μm .

Figure 6 shows final droplet radius as a function of the dry CCN radius for the three vertical velocities from Fig. 3. The figure illustrates the sharp separation for the 200 cm^{-3} simulations between activated CCN (that grow into cloud droplets) and inactivated CCN, with the separation radius smaller for larger updrafts as expected. The separation becomes less apparent for 2000 cm^{-3} weak-updraft simulations, in agreement with the discussion above. Because the largest CCN are activated first, droplets corresponding to large dry CCN have more time to grow after activation, and thus they have larger final radii than droplets corresponding to small dry CCN. This explains the finite spectral width as shown in Fig. 3. Finally, each dry CCN bin is either activated or remains as the inactivated (haze) CCN. This will change when turbulence is present as one might expect based on G22 single-size CCN simulations.

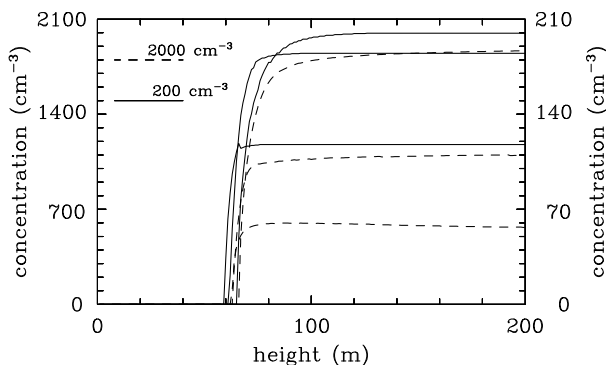


FIG. 4. Evolution of cloud droplet concentration in simulations from Fig. 3. Solid and dashed lines are 200 and 2,000 cm^{-3} simulations, with vertical scale on right and left sides, respectively. Lower, middle, and upper lines are for simulations with mean ascent of 0.25, 1, and 4 m s^{-1} , respectively.

5. CCN activation in the adiabatic turbulent parcel

The main set of simulations in the next subsection is for the 64^3-m^3 domain and TKE dissipation rate of $10^{-3} \text{ m}^2 \text{ s}^{-3}$ as in G22. That set corresponds exactly to the adiabatic parcel simulations from the previous section, that is, assuming the same mean ascent rates for either 200 or 2000 cm^{-3} simulations. Results from two additional sets of sensitivity simulations are presented in section 5b. The first set (for both 200 and 2000 cm^{-3} simulations) assumes two orders of magnitude lower dissipation rate, $10^{-5} \text{ m}^2 \text{ s}^{-3}$, and the same 64^3-m^3 domain. The second set

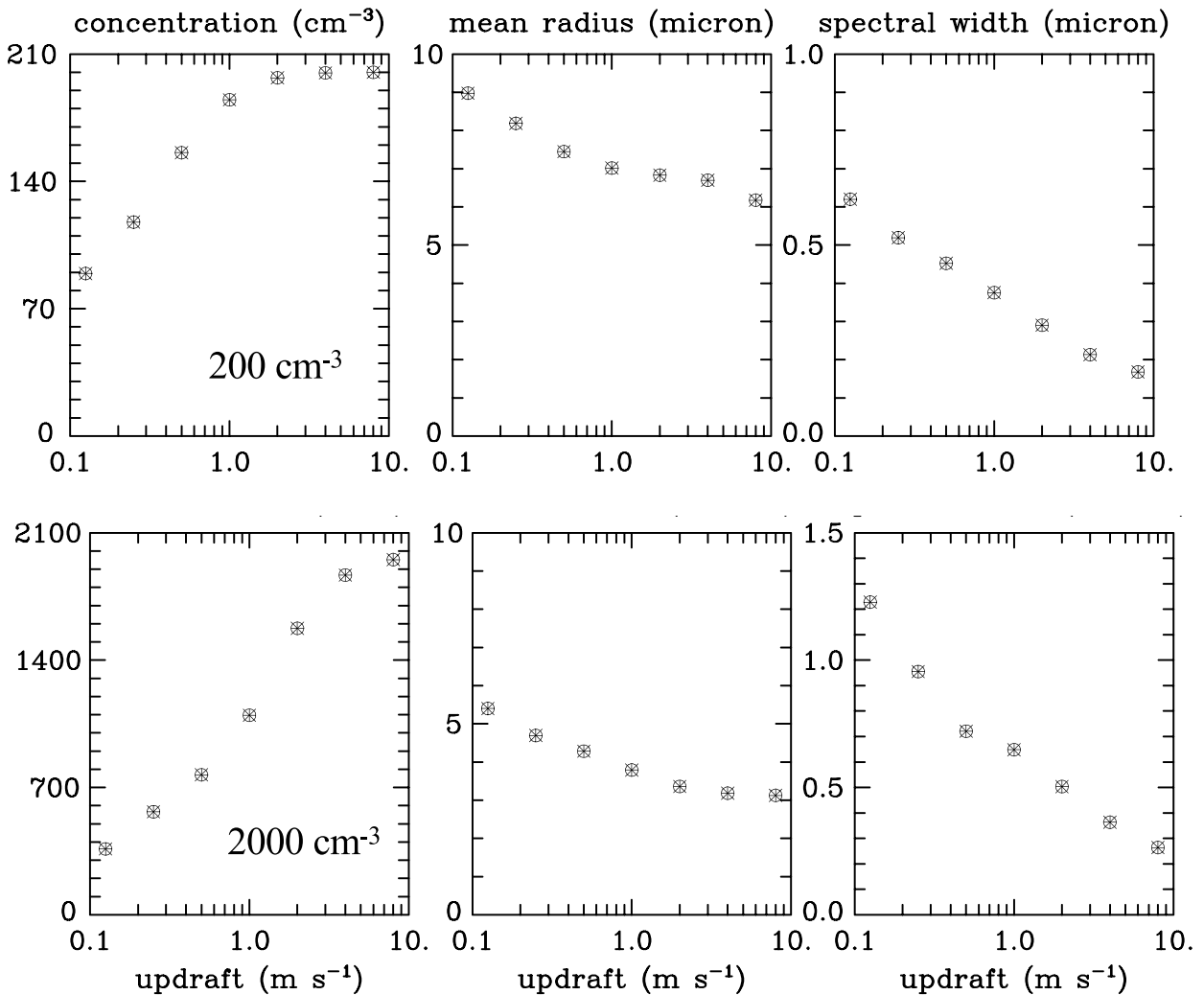


FIG. 5. (left) Concentration, (center) mean radius of activated droplets, and (right) spectral width at 200-m height as a function of the mean ascent for adiabatic parcel simulations. (top) 200 and (bottom) 2000 cm⁻³ simulations.

(again, for both 200 and 2000 cm⁻³ simulations) assumes a significantly smaller computational domain, 8³ m³, and the TKE dissipation rate of 10⁻³ m² s⁻³ (i.e., as in the main set). The appropriate scaling between the TKE E , the domain size L , and the TKE dissipation rate ε is $E \sim (L\varepsilon)^{2/3}$ [Pope 2000; Eq. (4) in Thomas et al. 2020]. Since the TKE (and thus velocities) are dominated by the large (i.e., domain-size) eddies, maximum velocities in the simulations with the lower TKE dissipation rate are about 5 times smaller ($100^{1/3} = 4.6$). For the simulations applying 8³ m³ computational domain, the maximum velocities are 2 times smaller ($8^{1/3} = 2$). However, the temperature perturbations (and thus the supersaturation perturbations) prior to the activation onset are expected to be 8 times smaller in agreement with the reduction of the domain vertical extent (see Fig. A2 in the G22 appendix).

a. Main set of adiabatic turbulent parcel simulations

Figure 7, in the format similar to Fig. 3, shows evolutions of the mean (i.e., domain-averaged) supersaturation and its spatial

distribution standard deviation, together with evolutions of the mean droplet radius and spectral width for the three parcel ascent rates of 0.25, 1 and 4 m s⁻¹. Compared to the nonturbulent parcel, the maxima of the mean supersaturation are smaller for the two lower ascent rates. The supersaturation standard deviations increase from zero at the start of the simulations to the maximum reached during the activation, with the largest increase with height for the smallest ascent rate. An explanation suggested in G22 involves time available to develop supersaturation fluctuations prior to CCN activation onset that is longer when the ascent rate is smaller. Note that—as argued in G22—the supersaturation fluctuations come from temperature fluctuations in large (i.e., domain-size) eddies and thus they develop on a time scale comparable to the large eddy turnover time. Considering the domain size (64³ m³) and vertical velocity maxima (between 0.5 and 0.8 m s⁻¹), the time scale is between 1 and 2 min. This is comparable to the parcel travel time between the initial height and the saturation level for 1 m s⁻¹

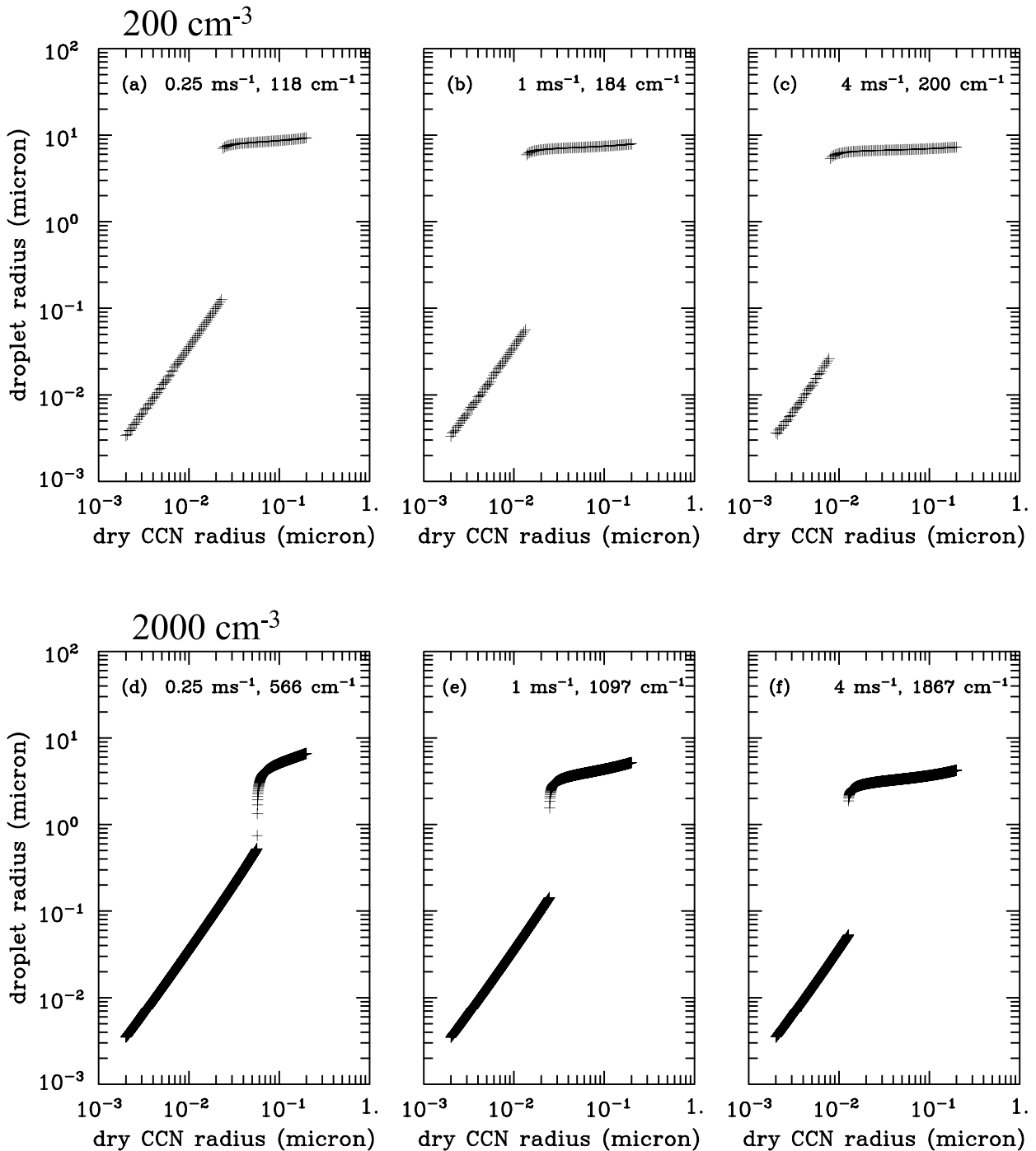


FIG. 6. Deliquesced CCN/droplet radius as a function of the dry CCN radius for simulations with (a),(d) 0.25 ; (b),(e) 1 ; and (c),(f) 4 m s^{-1} . (top) 200 and (bottom) 2000 cm^{-3} simulations. The number in each panel show final droplet concentration. Note the 10-times-larger number of bins in the 2000 cm^{-3} simulations.

mean ascent, and it is longer (shorter) than the travel time for higher (lower) mean ascent. Because the supersaturation standard deviation increase comes from turbulent temperature fluctuations prior to CCN activation, it is similar in corresponding mean ascents for 200 and 2000 cm^{-3} cases. For the 0.25 m s^{-1}

ascent rate, the activation starts before the mean saturation is reached. This shows the key role of supersaturation fluctuations in the CCN activation (Prabhakaran et al. 2020). Because concentration of cloud droplets increases with the mean ascent rate increase, droplets are larger for the weak ascent. The mean

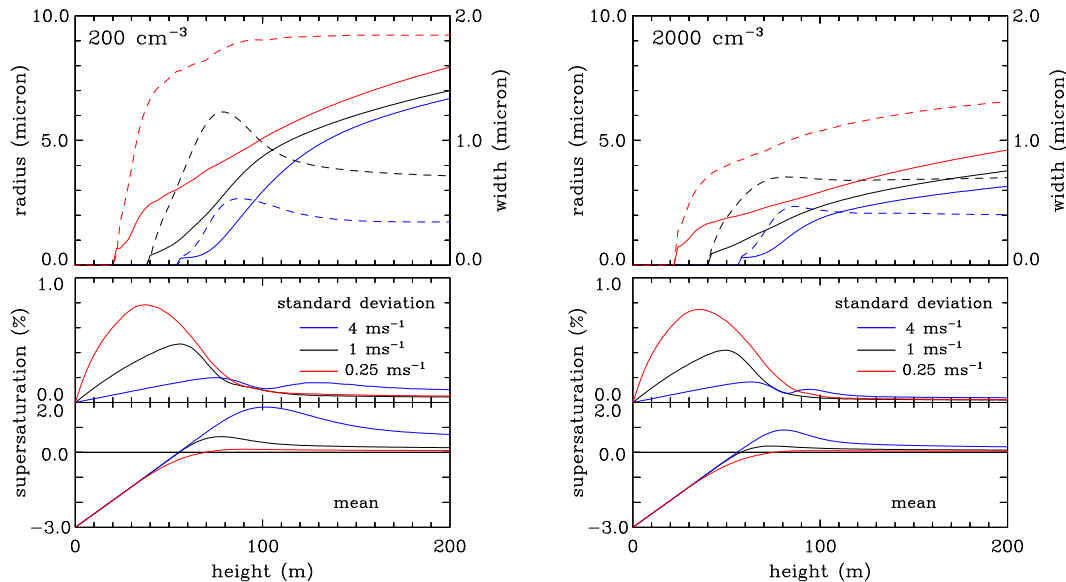


FIG. 7. (bottom) Evolutions of mean supersaturation and standard deviation of supersaturation spatial distribution. (top) Evolutions of mean droplet radius (solid lines; left scale on vertical axis) and spectral width (dashed lines; right scale on vertical axis) for turbulent 64^3 m^3 parcel simulations with TKE dissipation of $10^{-3} \text{ m}^2 \text{ s}^{-3}$. Updraft velocities of 0.25, 1, and 4 m s^{-1} are shown by different line colors. (left) 200 and (right) 2000 cm^{-3} simulations.

droplet radii at 200-m height are similar with (Fig. 7) and without (Fig. 3) turbulence.

Spectral width evolutions in Figs. 3 and 7 have some similarities between corresponding cases with and without turbulence. However, significant differences are apparent, such as more gradual changes with height and overall larger values for the corresponding cases when effects of turbulence are included. Spectral width after activation either remains almost constant or slowly increase in a way similar to the weak updraft 2000 cm^{-3} nonturbulent cases. All these are not unexpected as turbulence provides variability among individual CCN/droplet trajectories as documented in the subsequent figures. Differences in the spectral width evolutions between nonturbulent and turbulent cases shortly after activation come from the key role of different growth histories provided by the cloud turbulence (Cooper 1989). They bring to mind differences seen in stochastic model simulations and the “eddy hopping argument” in Grabowski and Abade (2017, see their Figs. 2 and 3) as well as in Abade et al. (2018, see their Fig. 5). Evolutions of the mean droplet concentrations (explaining evolutions of the spectral width) show features similar to those for the nonturbulent parcel (Fig. 4) and thus are not shown.

Figure 8, in the format of Fig. 5, documents the mean activated droplet concentration and radius together with the mean spectral width at the final height of the simulation, 200 m, as a function of the mean ascent rate. Overall, results in Fig. 8 are similar to those for the nonturbulent parcel, with the exception of significantly larger spectral widths for the turbulent parcel. The latter is explained by Fig. 9 (in the format of Fig. 6) that uses 5% of the superdroplet population to show scatterplots of the CCN/droplet radius at the final 200-m height. In contrast to the nonturbulent parcel, turbulence provides a blurred separation

between activated and inactivated (haze) CCN, especially for weak updrafts. The blurriness comes from the presence of turbulent fluctuations that allow CCN bins to feature CCN/droplets at various stages of their evolution: unactivated (haze) CCN, CCN growing toward activation or evaporating toward deactivation, and activated CCN growing as cloud droplets. These are reminiscent of single-size CCN simulations in G22. There are also arguably less significant differences between 200 and 2000 cm^{-3} cases, such as activation of smaller CCN in the 200 cm^{-3} cases in agreement with the higher mean supersaturations in those cases (see Figs. 3 and 7).

Figure 10 is another way to document the impact of turbulence on CCN activation. The figure shows the fraction of activated CCN as a function of the dry CCN radius for all mean updraft velocities considered, from 0.125 to 8 m s^{-1} , at the final 200-m height. The fraction is calculated as the ratio of the droplet concentration (i.e., including only droplets larger than the activation radius) and the CCN concentration for a given dry CCN bin. The blurred boundary between activated and inactivated CCN moves toward smaller CCN when the updraft increases as already documented in Fig. 9. Moreover, as the mean updraft increases, the boundary between activated and inactivated CCN becomes less blurred. Another peculiar feature of Fig. 10 is that not all large CCN are activated, especially for the 2000 cm^{-3} case. For the weakest updraft, 0.125 m s^{-1} , activation fraction is below 100% for all classes for both 200 and 2000 cm^{-3} simulations. It is close to zero for the largest CCN and 2000 cm^{-3} weak updraft simulations. The reason for not activating all CCN in some bins is that CCN can activate and then deactivate when the mean supersaturation and supersaturation fluctuations are comparable. This is especially true for the polluted weak updraft cases.

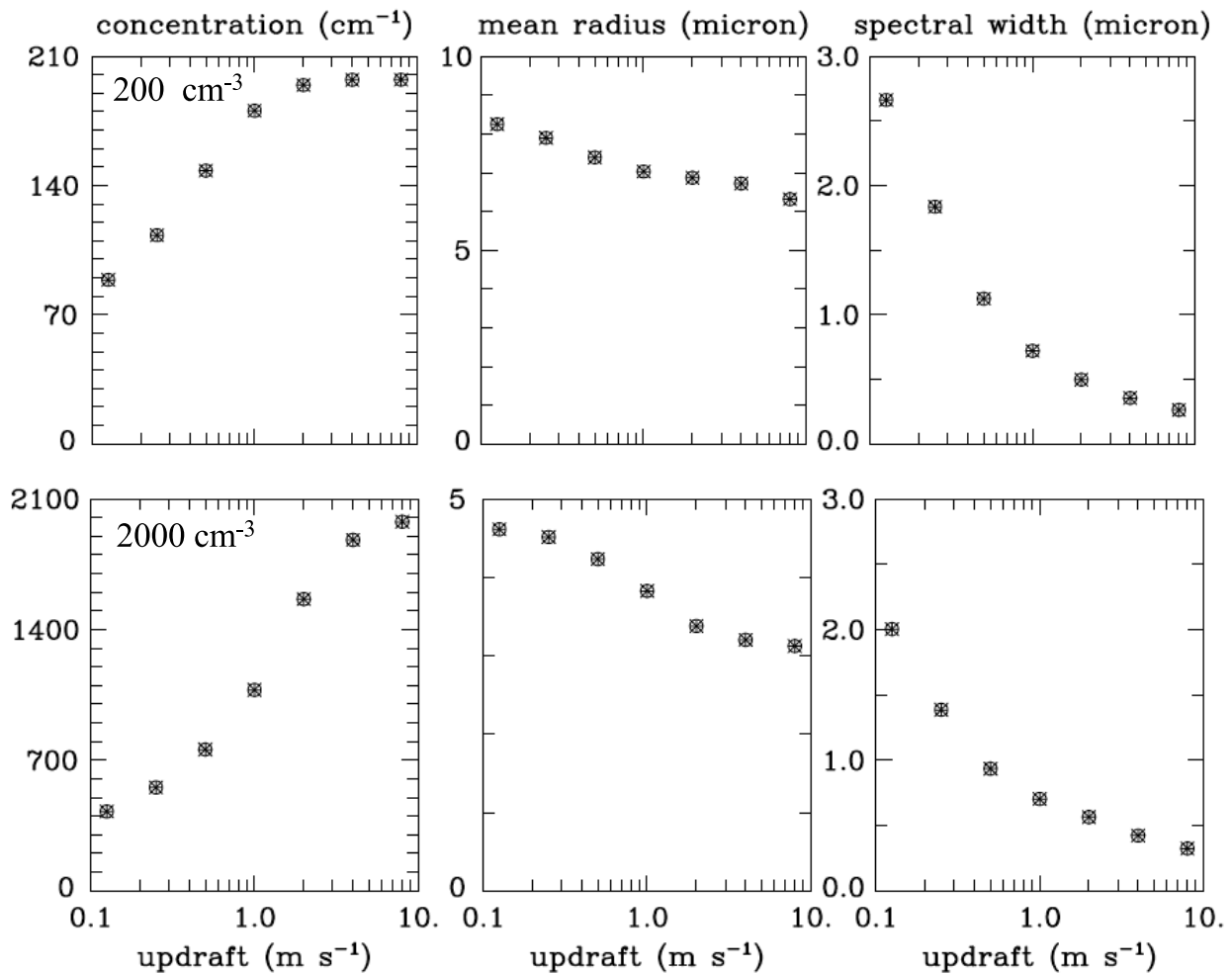


FIG. 8. As in Fig. 5, but for turbulent 64^3 m^3 parcel and TKE dissipation of $10^{-3} \text{ m}^2 \text{ s}^{-1}$.

For the illustration, Fig. 11 documents activation and subsequent deactivation of CCN in the CCN bin that feature 22-nm dry radius (i.e., close to the peak in the distribution, see Fig. 2). The activation radius is 190 nm ($0.19 \mu\text{m}$) as shown by the horizontal dashed line in the figure. The data come from 200 cm^{-3} simulation with 1 m s^{-1} updraft. In this case, 99.9% CCN within that bin become activated. From the 0.1% of the inactivated CCN, about half gets activated and then deactivated, and the other half is never activated. Some of those activated reach radii significantly larger than the activation radius and stay activated for a few seconds (several meters of the parcel rise), only to eventually evaporate and deactivate. Some go through this cycle more than once. For the same CCN bin and 0.5 m s^{-1} updraft, about 20% of the CCN remain inactivated at 200-m height, with about a third following activation and deactivation cycle. That number increases to 60% for the 0.25 m s^{-1} updraft, with again about a third activated and later deactivated.

b. Sensitivity simulations

The two sensitivity simulation sets feature either two orders of magnitude smaller TKE dissipation rate ($10^{-5} \text{ m}^2 \text{ s}^{-3}$) and

the same 64^3 m^3 domain (referred to as “very low TKE” in the figures) or the computational domain of 8^3 m^3 and the TKE dissipation rate as in the main set ($10^{-3} \text{ m}^2 \text{ s}^{-3}$). The second set is referred to as “ 8^3 m^3 domain” in the figures. Because the results are fairly similar to those discussed so far, we only present selected results for the 200 cm^{-3} set. Figure 12 shows the spectral width at the 200-m height as a function of the mean updraft strength, similarly to the upper right panel in Fig. 8. Plots for the droplet concentration and the mean radius are close to those in Fig. 8, and thus are not shown. Spectral widths in both sets are smaller than in 200 cm^{-3} simulations from the previous section, but they are still larger than in the case of the nonturbulent parcel.

Finally, Fig. 13, in the format of Fig. 10, shows the fraction of activated CCN as a function of the dry CCN radius for all mean updraft velocities considered at the final 200-m height. Overall, the pattern shown in the figure is similar to those shown in Fig. 10. First, increasing the mean updraft results in a shift of the boundary between activated and inactivated CCN toward smaller CCN, similar in left and right panels. Second, as the mean updraft speed decreases, the boundary between

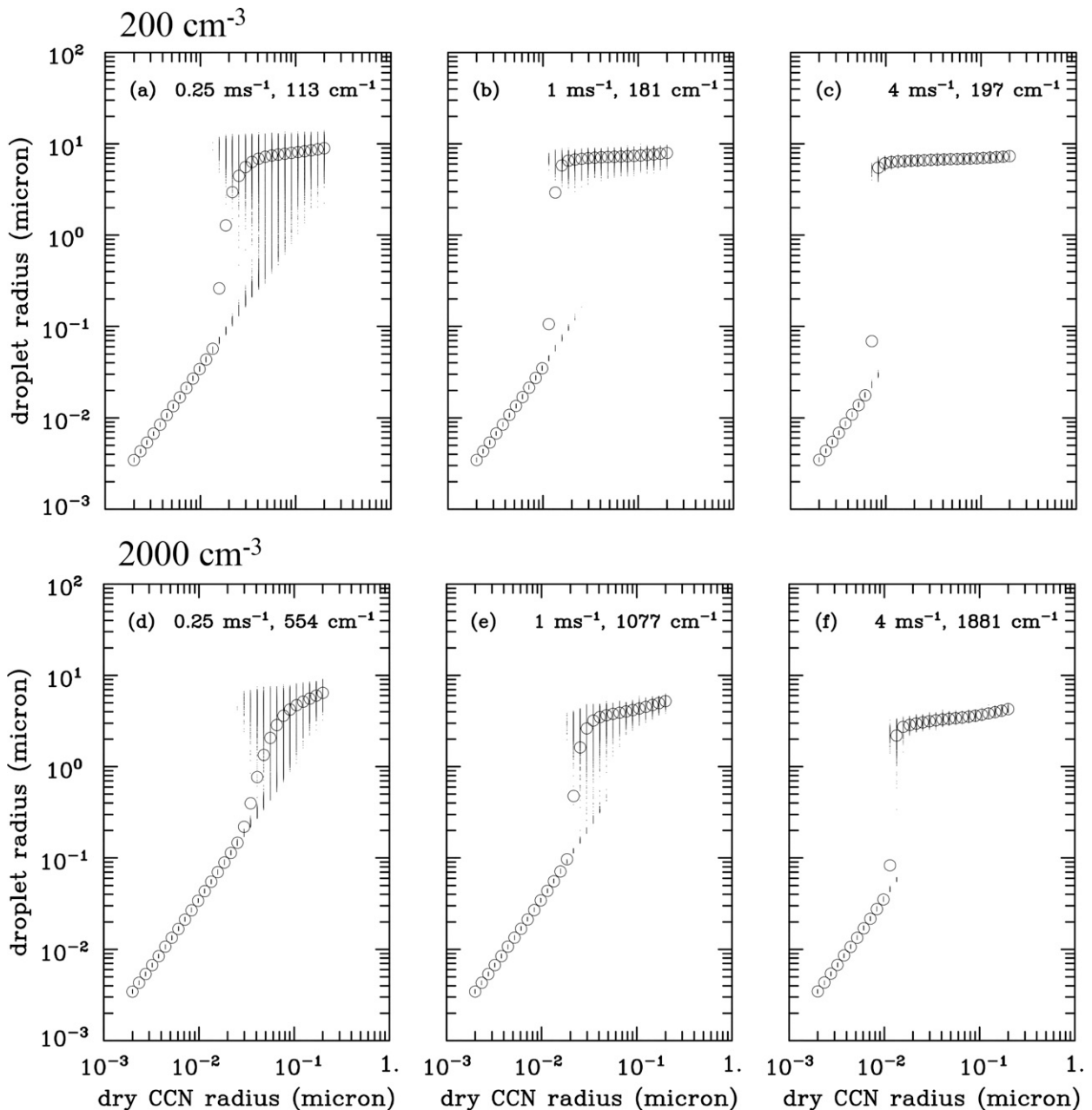


FIG. 9. As in Fig. 6, but for turbulent 64^3 m^3 parcel and with TKE dissipation of $10^{-3} \text{ m}^2 \text{ s}^{-3}$. For clarity, only 5% points are shown for each bin. Circles show the mean radius for each CCN dry radius bin.

activated and inactivated CCN becomes more blurred. The blurriness for weak updrafts appears the same in the left and right panels in Fig. 13, but it is smaller than in Fig. 10.

Overall, results of the sensitivity simulations show that both the TKE intensity and the computational domain size affect details of the simulated turbulence impact on CCN activation and the initial growth of cloud droplets. However, the key effects, such as the decreasing blurriness separating activated and inactivated CCN with the mean ascent increase, remain unaffected.

6. Discussion

Numerous cloud observations (starting with Warner 1969) and numerical simulations (e.g., Stevens et al. 1996; Lasher-Trapp et al. 2005) show that the cloud updraft is not uniform across the cloud base. It follows that even without effects of small-scale turbulence, activated droplet spectra vary above the cloud base between locations with weaker and stronger cloud-base updrafts. If such droplet populations are mixed above the cloud base, the spectra may exhibit complex structures. This has been referred

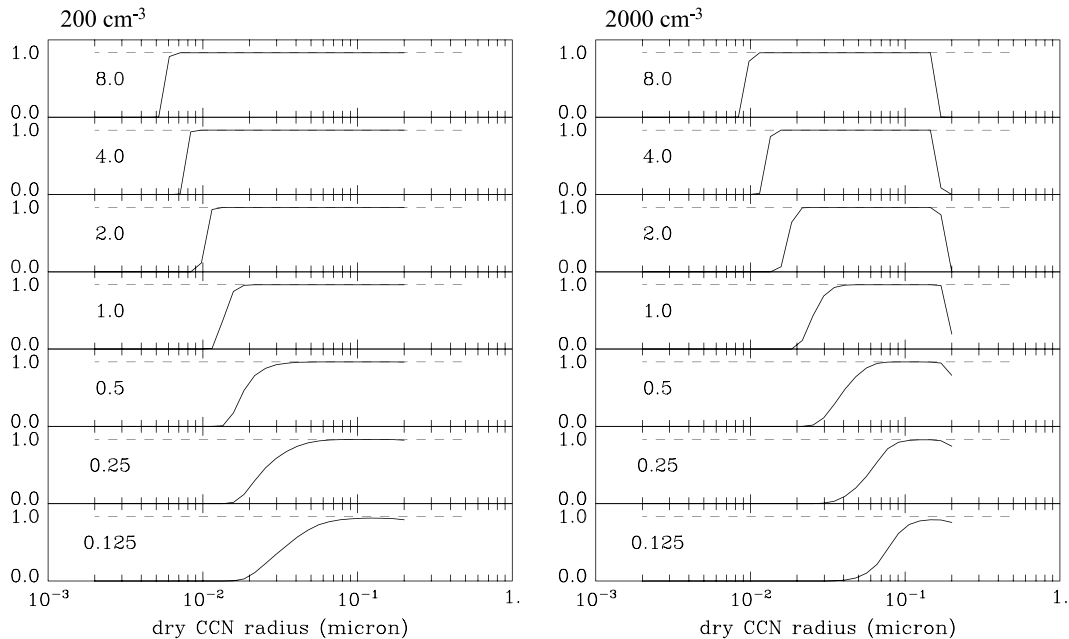


FIG. 10. Activation fraction as a function of the dry CCN radius for different mean ascent rates are shown in each panel. The thin dashed lines show the activation fraction equal to 1. Data for turbulent 64^3 m^3 parcel and TKE dissipation of $10^{-3} \text{ m}^2 \text{ s}^{-3}$. (left) 200 and (right) 2000 cm^{-3} simulations.

to as “internal mixing” in Hudson and Svensson (1995) and as “differential activation” in Stevens et al. (1996). Our results, although related in some general sense to those studies, are more along the line of variable droplet growth histories in a turbulent environment (e.g., Cooper 1989; Lasher-Trapp et al. 2005) and the “eddy hopping mechanism” as discussed in Grabowski and Abade (2017) and Abade et al. (2018).

The idealized simulations discussed here call for more realistic simulations of cloud-base activation, with a realistic spatial distribution of the updraft velocity (in horizontal and vertical)

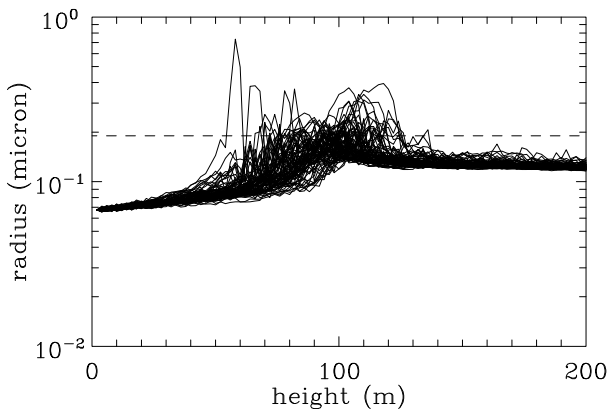


FIG. 11. Growth histories of CCN from 22-nm bin that remain inactivated at the 200-m height in turbulent 64^3 m^3 parcel and TKE dissipation of $10^{-3} \text{ m}^2 \text{ s}^{-3}$. Data from the 200 cm^{-3} simulation with a 1 m s^{-1} updraft. The dashed line shows the activation (critical) radius.

and turbulence characteristics. One possibility, already mentioned in G22, is to consider very high-resolution simulations of a cumulus congestus development similar to those discussed in Grabowski (2020b) and Chandrakar et al. (2021). Figure 14 shows example of results from one of simulations in the Chandrakar et al. (2021). The simulations apply LES setup following Lasher-Trapp et al. (2005) and Grabowski (2020b), and model development of a single cumulus cloud from a turbulent boundary layer driven by surface sensible and latent heat fluxes. The Chandrakar et al. (2021) simulations apply a 50-m grid length and use a subgrid-scale turbulence parameterization following Deardorff (1980). The parameterization, a standard approach applied in various convective-scale LES models, predicts evolution of the unresolved (subgrid-scale) TKE. It needs to be stressed that the TKE comes from the parameterization, not from resolved inertial-range turbulence dynamics as in ILES simulations discussed here. Nevertheless, Fig. 14 documents aspects relevant to the impact of turbulence on cloud-base CCN activation. The left panel of Fig. 14 shows a snapshot of the subgrid-scale TKE that is transported from the turbulent boundary layer in a plume originating near the surface. The shape of a cloud can be seen by a sharp boundary between close-to-zero TKE outside of the cloud and relatively high ($\sim 1 \text{ m}^2 \text{ s}^{-2}$) values inside the cloud. The in-cloud subgrid-scale TKE increases above the cloud base (located around 1200-m height), with the largest values near the very cloud top. The in-cloud TKE increase (over the TKE advected from the boundary layer) arguably comes from cloud-environment interfacial instabilities that drive cloud entrainment and dilution, see Grabowski and Clark (1993). Such a picture is consistent with in situ aircraft

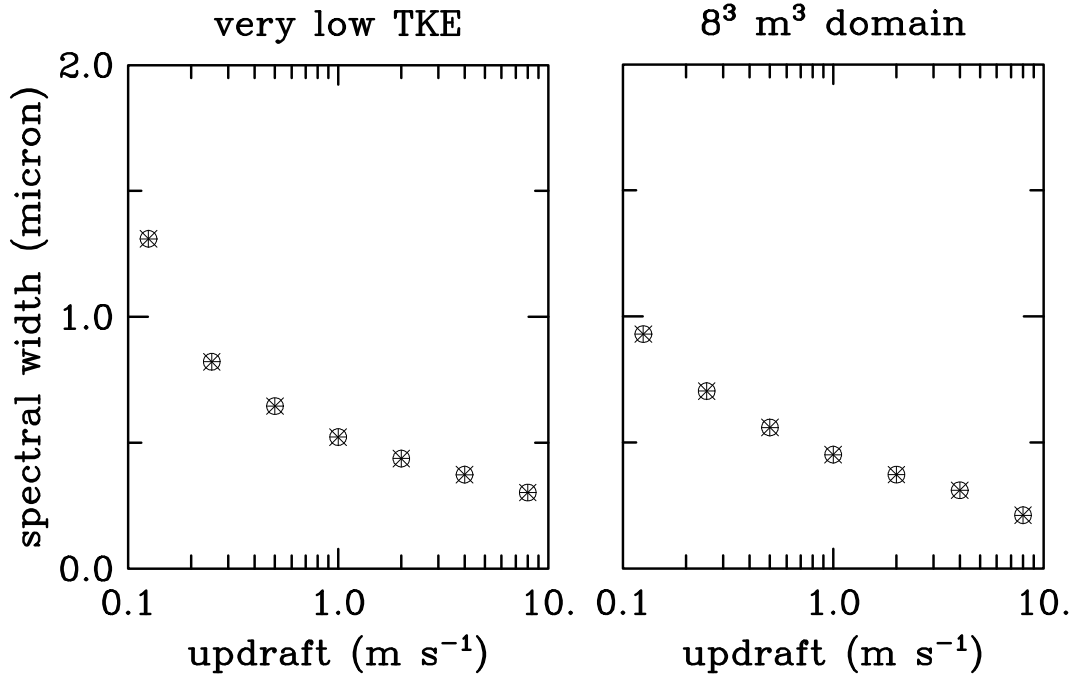


FIG. 12. Spectral width at 200-m height as a function of the mean ascent for (left) turbulent 64³ m³ parcel and TKE dissipation of 10⁻⁵ m² s⁻³ and (right) turbulent 8³ m³ parcel and TKE dissipation of 10⁻³ m² s⁻³. For the 200 cm⁻³ simulations only.

observations of small cumuli developing from the turbulent boundary layer. An important feature is that the simulated subgrid-scale TKE is not uniform across the cloud base. This is documented in the right panel that shows a scatterplot of

the TKE versus the local updraft velocity for heights in the 1000–1500-m range, that is, near the cloud base. The most points are in the updraft range from 0.1 to 1 m s⁻¹ and TKE between a few hundredths and 0.1 m² s⁻². The updraft and

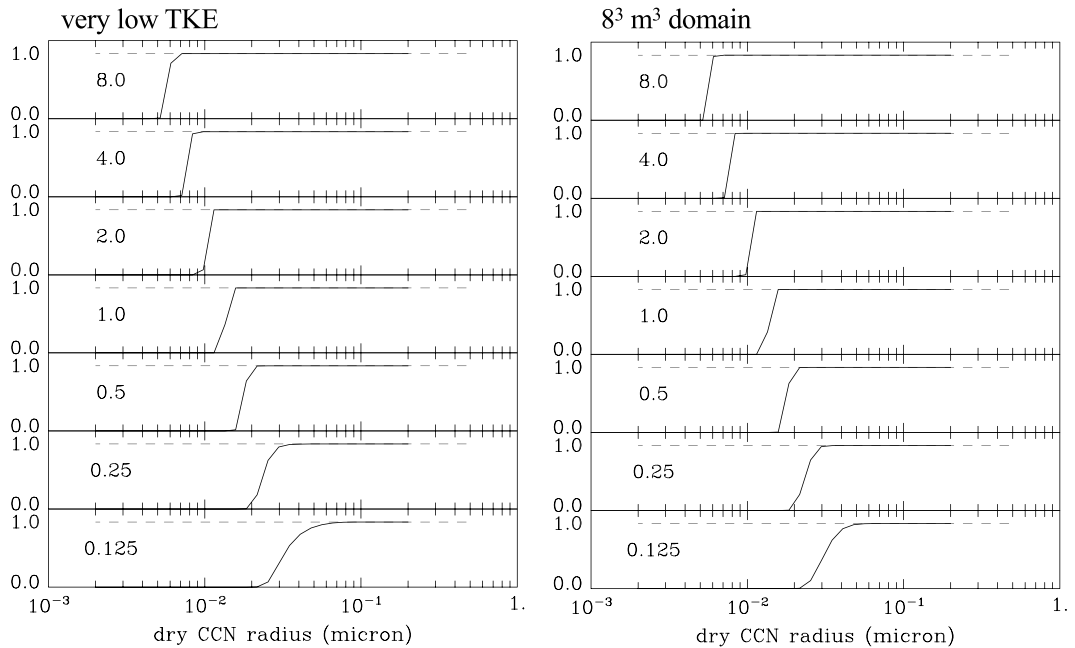


FIG. 13. As in Fig. 8, but (left) turbulent 64³ m³ parcel and TKE dissipation of 10⁻⁵ m² s⁻³, and (right) turbulent 8³ m³ parcel and TKE dissipation of 10⁻³ m² s⁻³. For the 200 cm⁻³ simulations only.

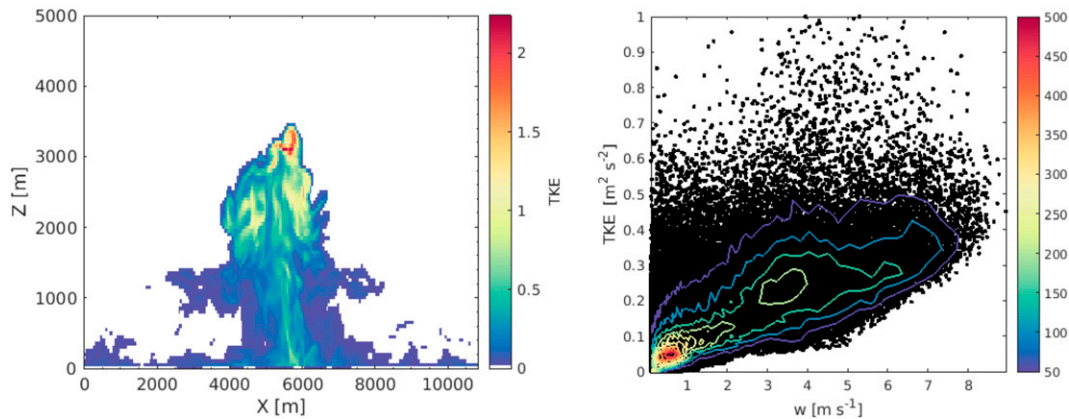


FIG. 14. Results from cloud simulations of Chandrakar et al. (2021). (left) Map of the predicted TKE (color scale; in $\text{m}^2 \text{s}^{-2}$) at the center cloud through the developing congestus cloud at 117 min of the simulation CTR. Cloud base is located at around 1200-m height. (right) Point-by-point comparison of the predicted TKE vs local updraft strength. Data come from seven snapshots of the simulation between 111 and 117 min. Only data for levels near the cloud base (1000–1500-m height) with the vertical velocity larger than 0.1 m s^{-1} are included. Color contours mark the number of points with the color scale to the right of the panel.

TKE values considered in the simulations discussed in this paper fall within such a range. However, there are also grid volumes with significantly higher TKE values, most below $0.5 \text{ m}^2 \text{ s}^{-2}$, that is, an order of magnitude higher than considered for ILES simulations here (note that the cloud model grid volume of 50^3 m^3 is similar to the 64^3 m^3 volume considered in most simulations here). Another aspect relevant to the idealized turbulence simulations discussed in this paper is that there seems to be a general relationship between the simulated local updraft velocity and the predicted TKE. This suggests that our main assumption of the separation between the mean updraft and the TKE (as in other previous studies, such as Clark and Hall 1979; Grabowski and Abade 2017; Abade et al. 2018) may not be generally valid in natural clouds.

The blurriness of the separation between activated and inactivated (haze) CCN is reminiscent of the observations in the Michigan Tech laboratory apparatus, the Pi chamber (Prabhakaran et al. 2020; Shawon et al. 2021). However, their reference to the blurriness concerns partitioning between activated and inactivated single-size CCN, and thus it is relevant to numerical simulations in G22. The blurriness in our simulations concerns a gradual change of the activation fraction, the ratio of the activated to the total CCN concentration for a given dry CCN size, across the CCN distribution (see Figs. 10 and 13). The decreasing activation fraction with the decrease of the dry CCN radius arguably represents a transition from the mean-dominated activation for the activation fraction of 1 for large CCN, through the fluctuation-influenced CCN activation at intermediate activation fractions, down to the fluctuation-dominated CCN activation for small activation fractions. Decreasing blurriness with the increase of the updraft speed represents narrowing of the range of dry CCN bins over which the transition from the mean-dominated to the fluctuation-dominated CCN activation takes place. The decrease

of the blurriness range is likely a result of the reduction of time it takes the parcel to cross the cloud base.

7. Summary

Following simulations of single-size CCN activation in Grabowski et al. (2022, hereafter G22), this study considers turbulence effects on the cloud droplet formation near the cloud base in the case of the CCN distribution. We consider a realistic (i.e., obtained from field measurements) CCN size distribution that features two lognormal modes centered at 20 and 75 nm (0.020 and 0.075 μm , respectively), the geometric standard deviations of 1.4 and 1.6 (unitless), and total concentrations of 120 and 80 cm^{-3} , respectively; see Fig. 2. The distribution is truncated to cover only the range between 2 and 200 nm (0.002 and 0.2 μm) because CCN concentrations outside the assumed range are small. The truncated size distribution is used with the total concentration of either 200 or 2000 cm^{-3} to contrast CCN activation in clean and polluted environments. As in G22, CCN is assumed to be sodium chloride.

We contrast activation within an adiabatic rising parcel without turbulence (i.e., as in traditional CCN activation studies) with activation taking place when the adiabatic parcel is filled with homogeneous isentropic inertial-range turbulence. The turbulent parcel is simulated by a rising cubic computational domain that is periodic in all three directions exactly as in G22 (see their Fig. A1). The main set of simulations applies the computational domain of 64^3 m^3 and the TKE dissipation rate of $10^{-3} \text{ m}^2 \text{ s}^{-3}$. This is a relatively low TKE dissipation rate, arguably appropriate for the turbulence carried by the rising air parcel from the subcloud layer (e.g., Siebert et al. 2006; Borque et al. 2016). Because the domain size determines amplitude of the supersaturation fluctuations prior to the CCN activation, and the turbulence intensity impacts cloud droplet growth after activation, two sets of sensitivity simulations are also considered. In

the first set, the TKE dissipation rate is assumed even lower ($10^{-5} \text{ m}^2 \text{ s}^{-3}$) with the same 64^3 m^3 domain. The second set features a significantly smaller computational domain, 8^3 m^3 , and the TKE dissipation rate of $10^{-3} \text{ m}^2 \text{ s}^{-3}$ (i.e., as in the main set). In contrast to adiabatic parcel simulations that typically focus on the relationship between CCN characteristics and the concentration of activated droplets (e.g., Ghan et al. 2011 and references therein), we document the evolution of the spectral width during and immediately after the activation.

For droplet concentrations and mean radii after activation, simulations with nonturbulent and turbulent parcels provide similar results, especially for stronger updrafts (see Figs. 5 and 8). The spectral width for the nonturbulent parcel and pristine CCN conditions (200 cm^{-3} simulations) decreases after activation, reaching values of a few tenths of $1 \mu\text{m}$ at the 200-m height. For similar simulations with polluted conditions (2000 cm^{-3} simulations), spectral width keeps increasing for ascent rates smaller than 1 m s^{-1} . This is because activation is still not completed at the 200-m height, see concentration evolutions in Fig. 4. This can be explained by a slow growth of deliquesced CCN when the local supersaturation is barely above the equilibrium supersaturation, or evaporation of droplets having radius larger than the activation radius when the local supersaturation becomes smaller than the equilibrium supersaturation.

Analogous spectral width evolutions are simulated for the adiabatic turbulent parcel, with the key difference of significantly larger spectral widths at 200 m for the turbulent parcel and for both 200 and 2000 cm^{-3} total CCN concentrations. Significantly broader droplet spectra after CCN turbulent activation provide an early start for the expected further increase of the spectral width due to turbulence impact on the droplet growth as discussed in Lanotte et al. (2009), Sardina et al. (2015, 2018), Grabowski and Abade (2017), Abade et al. (2018), Li et al. (2019), Thomas et al. (2020), and Grabowski and Thomas (2021). The increased spectral width in turbulent simulations comes from the blurriness of the boundary between activated and inactivated dry CCN bins that is especially evident for weak updrafts (Figs. 9 and 10). This is because a weak updraft provides a long time needed for the parcel to cross the cloud base and enables CCN activation and subsequent deactivation in the fluctuating supersaturation (see Fig. 11). Although not as pronounced as in the main set of simulations, the blurriness is evident in the sensitivity simulations as well (Fig. 13). The activation followed by deactivation also affects large CCN in the polluted case 64^3 m^3 higher-TKE simulations (see Fig. 10 right panel). Leaving some CCN inactivated above the cloud base when compared to the nonturbulent parcel allows additional activation above the cloud base when the supersaturation (the mean plus the turbulent perturbation) surpasses the critical supersaturation (for instance, because of the increasing cloud updraft velocity).

The above considerations call for high resolution ($\sim 1 \text{ m}$, as in ILES simulations here) cloud simulations focusing on the turbulent cloud-base CCN activation. A recent study of Strauss et al. (2022) reports cumulus congestus simulations with a uniform grid length of 5 m applying bulk cloud microphysics. Arguably, simulations with similar grid lengths and a more advanced microphysics (for instance, as used in Chandrakar

et al. 2021) will be possible soon. We hope to report on such simulations in the future.

Acknowledgments. This material is based upon work supported by the National Center for Atmospheric Research, which is a major facility sponsored by the National Science Foundation under Cooperative Agreement 1852977. WWG acknowledges partial support from the U.S. DOE ASR Grant DE-SC0020118. We thank Dr. Kamal Kant Chandrakar for providing Fig. 14. Dr. Jeff Snider suggested several references pertinent to past observations of natural CCN and CCN activation studies. Comments on an early version of the manuscript by NCAR's Dr. Sisi Chen are acknowledged.

Data availability statement. Data supporting this study are available at https://dashrepo.ucar.edu/dataset/215_grabow.html (Grabowski 2021). The code for the simulations is available at https://www2.mmm.ucar.edu/people/grabowski/files/eulag_files.activation.con_S.1mps.csh.

REFERENCES

- Abade, G. C., W. W. Grabowski, and H. Pawlowska, 2018: Broadening of cloud droplet spectra through eddy hopping: Turbulent entraining parcel simulations. *J. Atmos. Sci.*, **75**, 3365–3379, <https://doi.org/10.1175/JAS-D-18-0078.1>.
- Andrejczuk, M., W. W. Grabowski, S. P. Malinowski, and P. K. Smolarkiewicz, 2004: Numerical simulation of cloud–clear air interfacial mixing. *J. Atmos. Sci.*, **61**, 1726–1739, [https://doi.org/10.1175/1520-0469\(2004\)061<1726:NSOCAI>2.0.CO;2](https://doi.org/10.1175/1520-0469(2004)061<1726:NSOCAI>2.0.CO;2).
- Arabas, S., and S.-I. Shima, 2017: On the CCN (de)activation non-linearities. *Nonlinear Processes Geophys.*, **24**, 535–542, <https://doi.org/10.5194/npg-24-535-2017>.
- Borque, P., E. Luke, and P. Kollias, 2016: On the unified estimation of turbulence eddy dissipation rate using Doppler cloud radars and lidars. *J. Geophys. Res. Atmos.*, **121**, 5972–5989, <https://doi.org/10.1002/2015JD024543>.
- Chandrakar, K. K., W. W. Grabowski, H. Morrison, and G. H. Bryan, 2021: Impact of entrainment-mixing and turbulent fluctuations on droplet size distributions in a cumulus cloud: An investigation using Lagrangian microphysics with a sub-grid-scale model. *J. Atmos. Sci.*, **78**, 2983–3005, <https://doi.org/10.1175/JAS-D-20-0281.1>.
- Clark, T. L., and W. D. Hall, 1979: A numerical experiment on stochastic condensation theory. *J. Atmos. Sci.*, **36**, 470–483, [https://doi.org/10.1175/1520-0469\(1979\)036<0470:ANEOSC>2.0.CO;2](https://doi.org/10.1175/1520-0469(1979)036<0470:ANEOSC>2.0.CO;2).
- Cooper, W., 1989: Effects of variable droplet growth histories on droplet size distributions. Part I: Theory. *J. Atmos. Sci.*, **46**, 1301–1311, [https://doi.org/10.1175/1520-0469\(1989\)046<1301:EOVDGH>2.0.CO;2](https://doi.org/10.1175/1520-0469(1989)046<1301:EOVDGH>2.0.CO;2).
- Deardorff, J. W., 1980: Stratocumulus-capped mixed layer derived from a three-dimensional model. *Bound.-Layer Meteor.*, **18**, 495–527, <https://doi.org/10.1007/BF00119502>.
- Ditas, F., R. A. Shaw, H. Siebert, M. Simmel, B. Wehner, and A. Wiedensohler, 2012: Aerosols-cloud microphysics-thermodynamics-turbulence: Evaluating supersaturation in a marine stratocumulus cloud. *Atmos. Chem. Phys.*, **12**, 2459–2468, <https://doi.org/10.5194/acp-12-2459-2012>.
- Dziekan, P., J. B. Jensen, W. W. Grabowski, and H. Pawlowska, 2021: Impact of giant sea salt aerosol particles on

- precipitation in marine cumuli and stratocumuli: Lagrangian Cloud Model simulations. *J. Atmos. Sci.*, **78**, 4127–4142, <https://doi.org/10.1175/JAS-D-21-0041.1>.
- Feingold, G., W. R. Cotton, S. M. Kreidenweis, and J. T. Davis, 1999: The impact of giant cloud condensation nuclei on drizzle formation in stratocumulus: Implications for cloud radiative properties. *J. Atmos. Sci.*, **56**, 4100–4117, [https://doi.org/10.1175/1520-0469\(1999\)056<4100:TIOGCC>2.0.CO;2](https://doi.org/10.1175/1520-0469(1999)056<4100:TIOGCC>2.0.CO;2).
- Fitzgerald, J. W., 1973: Dependence of the supersaturation spectrum of CCN on aerosol size distribution and composition. *J. Atmos. Sci.*, **30**, 628–634, [https://doi.org/10.1175/1520-0469\(1973\)030<0628:DOTSSO>2.0.CO;2](https://doi.org/10.1175/1520-0469(1973)030<0628:DOTSSO>2.0.CO;2).
- Ghan, S. J., and Coauthors, 2011: Droplet nucleation: Physically-based parameterizations and comparative evaluation. *J. Adv. Model. Earth Syst.*, **3**, M10001, <https://doi.org/10.1029/2011MS000074>.
- Grabowski, W. W., 2020a: Comparison of Eulerian bin and Lagrangian particle-based schemes in simulations of Pi Chamber dynamics and microphysics. *J. Atmos. Sci.*, **77**, 1151–1165, <https://doi.org/10.1175/JAS-D-19-0216.1>.
- , 2020b: Comparison of Eulerian bin and Lagrangian particle-based microphysics in simulations of nonprecipitating cumulus. *J. Atmos. Sci.*, **77**, 3951–3970, <https://doi.org/10.1175/JAS-D-20-0100.1>.
- , 2021: Turbulent activation of cloud condensation nuclei, version 1.0. UCAR/NCAR–DA Repository, accessed 12 October 2022, <https://doi.org/10.5065/z9wk-1x22>.
- , and T. L. Clark, 1993: Cloud–environment interface instability. Part II: Extension to three spatial dimensions. *J. Atmos. Sci.*, **50**, 555–573, [https://doi.org/10.1175/1520-0469\(1993\)050<0555:CEIIP1>2.0.CO;2](https://doi.org/10.1175/1520-0469(1993)050<0555:CEIIP1>2.0.CO;2).
- , and L.-P. Wang, 2009: Diffusional and accretional growth of water drops in a rising adiabatic parcel: Effects of the turbulent collision kernel. *Atmos. Chem. Phys.*, **9**, 2335–2353, <https://doi.org/10.5194/acp-9-2335-2009>.
- , and G. C. Abade, 2017: Broadening of cloud droplet spectra through eddy hopping: Turbulent adiabatic parcel simulations. *J. Atmos. Sci.*, **74**, 1485–1493, <https://doi.org/10.1175/JAS-D-17-0043.1>.
- , and L. Thomas, 2021: Cloud droplet diffusional growth in homogeneous isotropic turbulence: Bin microphysics versus Lagrangian superdroplet simulations. *Atmos. Chem. Phys.*, **21**, 4059–4077, <https://doi.org/10.5194/acp-21-4059-2021>.
- , M. Andrejczuk, and L.-P. Wang, 2011: Droplet growth in a bin warm-rain scheme with Twomey CCN activation. *Atmos. Res.*, **99**, 290–301, <https://doi.org/10.1016/j.atmosres.2010.10.020>.
- , L. Thomas, and B. Kumar, 2022: Impact of cloud base turbulence on CCN activation: Single size CCN. *J. Atmos. Sci.*, **79**, 551–566, <https://doi.org/10.1175/JAS-D-21-0184.1>.
- Grinstein, F. F., L. G. Margolin, and W. J. Rider, 2007: *Implicit Large Eddy Simulation: Computing Turbulent Fluid Dynamics*. Cambridge University Press, 562 pp.
- Hoppel, W. A., 1979: Measurement of the size distribution and CCN supersaturation spectrum of submicron aerosols over the ocean. *J. Atmos. Sci.*, **36**, 2006–2015, [https://doi.org/10.1175/1520-0469\(1979\)036<2006:MOTSDA>2.0.CO;2](https://doi.org/10.1175/1520-0469(1979)036<2006:MOTSDA>2.0.CO;2).
- Hudson, J. G., and G. Svensson, 1995: Cloud microphysical relationships in California marine stratus. *J. Appl. Meteor.*, **34**, 2655–2666, [https://doi.org/10.1175/1520-0450\(1995\)034<2655:CMRICM>2.0.CO;2](https://doi.org/10.1175/1520-0450(1995)034<2655:CMRICM>2.0.CO;2).
- , and S. S. Yum, 2002: Cloud condensation nuclei spectra and polluted and clean clouds over the Indian Ocean. *J. Geophys. Res.*, **107**, 8022, <https://doi.org/10.1029/2001JD000829>.
- Jiusto, J. E., 1967: Aerosol and cloud microphysics measurements in Hawaii. *Tellus*, **19**, 359–368, <https://doi.org/10.3402/tellusa.v19i3.9805>.
- Johnson, D. B., 1982: The role of giant and ultragiant aerosol particles in warm rain initiation. *J. Atmos. Sci.*, **39**, 448–460, [https://doi.org/10.1175/1520-0469\(1982\)039<0448:TROGAU>2.0.CO;2](https://doi.org/10.1175/1520-0469(1982)039<0448:TROGAU>2.0.CO;2).
- Köhler, H., 1936: The nucleus in and growth of hygroscopic droplets. *Trans. Faraday Soc.*, **32**, 1152–1161, <https://doi.org/10.1039/TF9363201152>.
- Lanotte, A. S., A. Seminara, and F. Toschi, 2009: Cloud droplet growth by condensation in homogeneous isotropic turbulence. *J. Atmos. Sci.*, **66**, 1685–1697, <https://doi.org/10.1175/2008JAS2864.1>.
- Lasher-Trapp, S. G., W. A. Cooper, and A. M. Blyth, 2005: Broadening of droplet size distributions from entrainment and mixing in a cumulus cloud. *Quart. J. Roy. Meteor. Soc.*, **131**, 195–220, <https://doi.org/10.1256/qj.03.199>.
- Li, X.-Y., G. Svensson, A. Brandenburg, and N. E. L. Haugen, 2019: Cloud-droplet growth due to supersaturation fluctuations in stratiform clouds. *Atmos. Chem. Phys.*, **19**, 639–648, <https://doi.org/10.5194/acp-19-639-2019>.
- Margolin, L. G., and W. J. Rider, 2002: A rationale for implicit turbulence modelling. *Int. J. Numer. Methods Fluids*, **39**, 821–841, <https://doi.org/10.1002/flid.331>.
- , —, and F. F. Grinstein, 2006: Modeling turbulent flow with implicit LES. *J. Turbul.*, **7**, 15, <https://doi.org/10.1080/14685240500331595>.
- Mészáros, E., 1968: On the size distribution of water soluble particles in the atmosphere. *Tellus*, **20**, 443–448, <https://doi.org/10.3402/tellusa.v20i3.10023>.
- Miao, Q., Z. Zhang, Y. Li, X. Qin, B. Xu, Y. Yuan, and Z. Gao, 2015: Measurement of cloud condensation nuclei (CCN) and CCN closure at Mt. Huang based on hygroscopic growth factors and aerosol number-size distribution. *Atmos. Environ.*, **113**, 127–134, <https://doi.org/10.1016/j.atmosenv.2015.05.006>.
- Pinsky, M., I. P. Mazin, A. Korolev, and A. Khain, 2013: Supersaturation and diffusional droplet growth in liquid clouds. *J. Atmos. Sci.*, **70**, 2778–2793, <https://doi.org/10.1175/JAS-D-12-077.1>.
- Politovich, M. K., and W. A. Cooper, 1988: Variability of supersaturation in cumulus clouds. *J. Atmos. Sci.*, **45**, 1651–1664, [https://doi.org/10.1175/1520-0469\(1988\)045<1651:VOTSIC>2.0.CO;2](https://doi.org/10.1175/1520-0469(1988)045<1651:VOTSIC>2.0.CO;2).
- Pope, S. B., 2000: *Turbulent Flows*. Cambridge University Press, 807 pp.
- Prabhakaran, P., A. S. M. Shawon, G. Kinney, S. Thomas, W. Cantrell, and R. A. Shaw, 2020: The role of turbulent fluctuations in aerosol activation and cloud formation. *Proc. Natl. Acad. Sci. USA*, **117**, 16 831–16 838, <https://doi.org/10.1073/pnas.2006426117>.
- Pruppacher, H. R., and J. D. Klett, 1997: *Microphysics of Clouds and Precipitation*. Springer Science & Business Media, 945 pp.
- Reutter, P., and Coauthors, 2009: Aerosol- and updraft-limited regimes of cloud droplet formation: Influence of particle number, size and hygroscopicity on the activation of cloud condensation nuclei (CCN). *Atmos. Chem. Phys.*, **9**, 7067–7080, <https://doi.org/10.5194/acp-9-7067-2009>.
- Sardina, G., F. Picano, L. Brandt, and R. Caballero, 2015: Continuous growth of droplet size variance due to condensation in turbulent clouds. *Phys. Rev. Lett.*, **115**, 184501, <https://doi.org/10.1103/PhysRevLett.115.184501>.
- , S. Poulain, L. Brandt, and R. Caballero, 2018: Broadening of cloud droplet size spectra by stochastic condensation:

- Effects of mean updraft velocity and CCN activation. *J. Atmos. Sci.*, **75**, 451–467, <https://doi.org/10.1175/JAS-D-17-0241.1>.
- Shawon, A. S. M., P. Prabhakaran, G. Kinney, R. A. Shaw, and W. Cantrell, 2021: Dependence of aerosol-droplet partitioning on turbulence in a laboratory cloud. *J. Geophys. Res. Atmos.*, **126**, e2020JD033799, <https://doi.org/10.1029/2020JD033799>.
- Siebert, H., K. Lehmann, and M. Wendisch, 2006: Observations of small-scale turbulence and energy dissipation rates in the cloudy boundary layer. *J. Atmos. Sci.*, **63**, 1451–1466, <https://doi.org/10.1175/JAS3687.1>.
- Squires, P., 1952: The growth of cloud drops by condensation. 1. General characteristics. *Aust. J. Sci. Res.*, **5**, 59–86, <https://doi.org/10.1071/CH9520059>.
- Stevens, B., G. Feingold, W. R. Cotton, and R. L. Walko, 1996: Elements of the microphysical structure of numerically simulated nonprecipitating stratocumulus. *J. Atmos. Sci.*, **53**, 980–1006, [https://doi.org/10.1175/1520-0469\(1996\)053<0980:EOTMSO>2.0.CO;2](https://doi.org/10.1175/1520-0469(1996)053<0980:EOTMSO>2.0.CO;2).
- Strauss, C., D. Ricard, and C. Lac, 2022: Dynamics of the cloud–environment interface and turbulence effects in a LES of a growing cumulus congestus. *J. Atmos. Sci.*, **79**, 593–619, <https://doi.org/10.1175/JAS-D-20-0386.1>.
- Thomas, L., W. W. Grabowski, and B. Kumar, 2020: Diffusional growth of cloud droplets in homogeneous isotropic turbulence: DNS, scaled-up DNS, and stochastic model. *Atmos. Chem. Phys.*, **20**, 9087–9100, <https://doi.org/10.5194/acp-20-9087-2020>.
- Warner, J., 1969: The microstructure of cumulus cloud. Part II. The effect on droplet size distribution of the cloud nucleus spectrum and updraft velocity. *J. Atmos. Sci.*, **26**, 1272–1282, [https://doi.org/10.1175/1520-0469\(1969\)026<1272:TMOCCP>2.0.CO;2](https://doi.org/10.1175/1520-0469(1969)026<1272:TMOCCP>2.0.CO;2).